NASA/TM–20260003488



Real-Time Air Flow Angle Data for Fixed-Wing Aircraft using a Small Onboard Flight Controller

Eugene A. Morelli

Emeritus Langley Associate
NASA Langley Research Center, Hampton, Virginia

May 2026

NASA STI Program Report Series

Since its founding, NASA has been dedicated to the advancement of aeronautics and space science. The NASA scientific and technical information (STI) program plays a key part in helping NASA maintain this important role.

The NASA STI program operates under the auspices of the Agency Chief Information Officer. It collects, organizes, provides for archiving, and disseminates NASA's STI. The NASA STI program provides access to the NTRS Registered and its public interface, the NASA Technical Reports Server, thus providing one of the largest collections of aeronautical and space science STI in the world. Results are published in both non-NASA channels and by NASA in the NASA STI Report Series, which includes the following report types:

- TECHNICAL PUBLICATION. Reports of completed research or a major significant phase of research that present the results of NASA Programs and include extensive data or theoretical analysis. Includes compilations of significant scientific and technical data and information deemed to be of continuing reference value. NASA counter-part of peer-reviewed formal professional papers but has less stringent limitations on manuscript length and extent of graphic presentations.

- TECHNICAL MEMORANDUM. Scientific and technical findings that are preliminary or of specialized interest, e.g., quick release reports, working papers, and bibliographies that contain minimal annotation. Does not contain extensive analysis.

- CONTRACTOR REPORT. Scientific and technical findings by NASA-sponsored contractors and grantees.

- CONFERENCE PUBLICATION. Collected papers from scientific and technical conferences, symposia, seminars, or other meetings sponsored or co-sponsored by NASA.

- SPECIAL PUBLICATION. Scientific, technical, or historical information from NASA programs, projects, and missions, often concerned with subjects having substantial public interest.

- TECHNICAL TRANSLATION. English-language translations of foreign scientific and technical material pertinent to NASA's mission.

Specialized services also include organizing and publishing research results, distributing specialized research announcements and feeds, providing information desk and personal search support, and enabling data exchange services.

For more information about the NASA STI program, see the following:

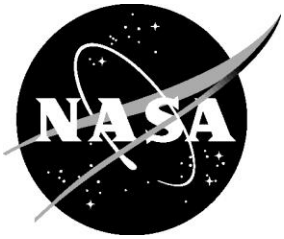
- Access the NASA STI program home page at http://www.sti.nasa.gov

- E-mail your question to help@sti.nasa.gov

- Phone the NASA STI Information Desk at 757-864-9658

- Write to:
  NASA STI Information Desk
  Mail Stop 148
  NASA Langley Research Center
  Hampton, VA 23681-2199

NASA/TM–20260003488



Real-Time Air Flow Angle Data for Fixed-Wing Aircraft using a Small Onboard Flight Controller

Eugene A. Morelli

Emeritus Langley Associate
NASA Langley Research Center, Hampton, Virginia

National Aeronautics and Space Administration

Langley Research Center
Hampton, Virginia 23681-2199

May 2026

The use of trademarks or names of manufacturers in this report is for accurate reporting and does not constitute an official endorsement, either expressed or implied, of such products or manufacturers by the National Aeronautics and Space Administration.

Available from:

NASA STI Program / Mail Stop 148
NASA Langley Research Center
Hampton, VA 23681-2199
Fax: 757-864-6500

Table of Contents

Abstract ii

Nomenclature iii

I. Introduction 1

II. Method 3

A. Air Flow Angle Models 4

1. Vertical Body-Axis Aerodynamic Force Model 4

2. Lateral Body-Axis Aerodynamic Force Model 6

B. Air Flow Angle Estimation 8

C. Dynamic Pressure 8

D. Real-Time Data Smoothing and Differentiation 9

E. Kinematic Reconstruction 13

F. Real-Time Air Flow Angle Model Calibration 15

G. Summary 18

III. Aircraft 19

A. F-16 Nonlinear Simulation 19

B. SEARCH-1 Subscale Aircraft 20

B. Cirrus SR-22 Aircraft 20

IV. Results 22

A. F-16 Nonlinear Simulation 22

B. Cirrus SR-22 Flight Test 24

V. Discussion 26

VI. Summary and Conclusions 30

Acknowledgments 30

References 31

Abstract

An algorithm was developed to estimate air flow angles (angle of attack and flank angle) for a fixed-wing aircraft in real time, using sensor data and computing capability available on a small onboard flight controller called the Pixhawk® Cube Orange. A realistic F-16 nonlinear simulation was used to develop and demonstrate the algorithm. Then the algorithm was demonstrated in flight using a piloted fixed-wing general aviation aircraft with a Pixhawk Cube Orange mounted inside the fuselage near the aircraft center of gravity. The flight test aircraft was equipped with calibrated air flow angle vane sensors installed on a wing boom to provide comparison data for the real-time air flow angle estimates. Flight test results showed that angle of attack and flank angle can be estimated accurately in real time using a Pixhawk Cube Orange, compared to calibrated vane sensor data. Vane sensors can incur errors from aircraft structural responses, local flow distortions, engine vibration, and adverse environmental effects such as ice and debris, along with errors from vane sensor calibration, vane inertia, and vane rotation friction. These error sources did not significantly affect the air flow angle estimates from the real-time algorithm implemented with the onboard Pixhawk Cube Orange, but mitigations were necessary to account for noise and biases in the sensor data from the Pixhawk Cube Orange. The novel flight-demonstrated concept described in this work provides a practical means for acquiring accurate air flow angle data in real time using a small, lightweight, and inexpensive Pixhawk Cube Orange mounted inside the aircraft fuselage.

®Pixhawk is a registered trademark of Dronecode Project, Inc. In this work, the simpler form Pixhawk is used for Pixhawk®.

Nomenclature

a_x, a_y, a_z	body-axis translational accelerometer measurements, g
b	wing span, ft
$\bar{c}$	mean aerodynamic chord, ft
C_Y, C_Z	nondimensional side and vertical body-axis aerodynamic force coefficients
C_m, C_n	nondimensional pitch and yaw body-axis aerodynamic moment coefficients
g	earth gravitational acceleration = 32.174 ft/s^2
I_x, I_y, I_z, I_{xz}	mass moments of inertia, slug-ft^2
m	aircraft mass, slug
N	number of data points
p, q, r	body-axis roll, pitch, and yaw angular velocity components, deg/s or rad/s
$\bar{q}$	dynamic pressure, lbf/ft^2
R	ideal gas constant for air = 1716.49 ft-lbf/slug-deg R
S	wing reference area, ft^2
V	true airspeed, ft/s
α	angle of attack, deg or rad
β	sideslip angle, deg or rad
β_f	flank angle, deg or rad
$\delta_e, \delta_a, \delta_r$	elevator, aileron, and rudder deflections, deg or rad
ϕ, θ, ψ	Euler roll, pitch, and yaw angles, deg or rad
ρ	air density, slug/ft^3

A. SUPERSCRIPTS

$\hat{}$	estimate
$\bar{}$	mean
$\dot{}$	time derivative
^{T}	transpose

B. SUBSCRIPTS

cg	center of gravity
o	reference or trim value

C. ACRONYMS

BL	Butt Line
FS	Fuselage Station
GPS	Global Positioning System
IMU	Inertial Measurement Unit
WL	Water Line

I. Introduction

Aircraft flight dynamics and performance depend strongly on the orientation of the aircraft with respect to the air-relative velocity vector. This orientation can be characterized by air flow angles called angle of attack α and flank angle β_f, as shown in Fig. 1. The definition of sideslip angle β is also illustrated in Fig. 1. Note that when the angle of attack is small, the flank angle and sideslip angle are nearly the same.

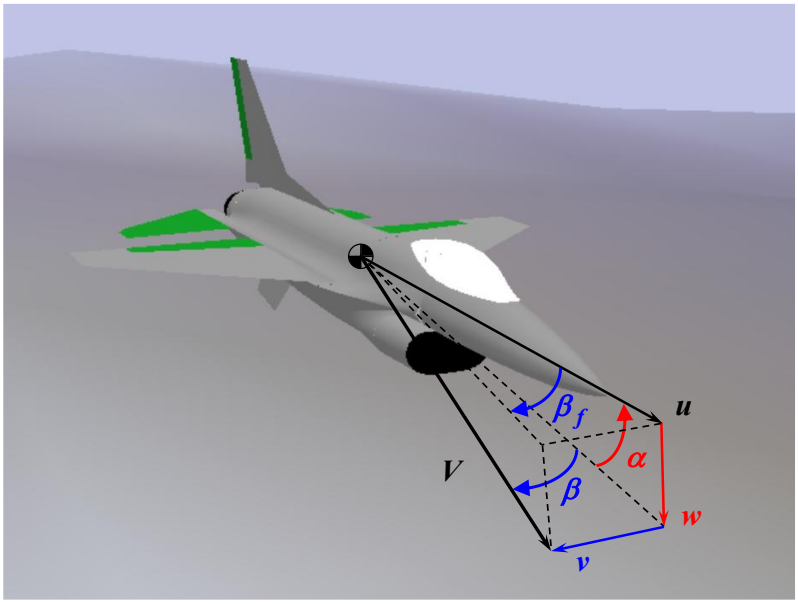


Figure 1. Air flow angles

The air flow angles are among the most difficult and expensive quantities to measure accurately on an aircraft in flight, because the aircraft creates local air disturbances as it flies, in a manner similar to the wake created by a boat moving through water. A sensor mounted near the aircraft body or wing will incur air flow angle measurement errors due to these local flow distortions. If the sensor is mounted away from the aircraft, then static and dynamic structural deflections of the airframe, wing, and mounting boom can adversely affect the accuracy of air flow angle measurements. In addition, for any sensor location different from the aircraft center of gravity, corrections are required to account for the rotational motion of the aircraft [1,2].

Air flow angles can be measured using vane sensors that are similar to weather vanes with a potentiometer on each rotation axis. Another approach is to use multiple pressure ports arranged in various configurations on the nose of the aircraft or on the nose of a probe mounted on the aircraft. The pressure measurements are calibrated using known air flow angles, often in a wind tunnel test or sometimes using computational fluid dynamics (CFD). These sensing approaches require relatively expensive hardware, along with extensive, careful, and time-consuming calibration to produce accurate air flow angle data [3].

From an aerodynamic standpoint, the best place for an air flow angle sensor is on a boom mounted to the nose of the aircraft, away from local flow distortion effects. However, this location is often not available because of a propeller or radar equipment, and still has the

structural dynamic motion problem due to the boom. Air flow angle instrumentation is also susceptible to adverse environmental conditions, such as rain, ice, snow, birds, insects, dirt, and debris. The sensors can be delicate and expensive to install and maintain in the flight environment. An additional risk is damage on the ground from impact with personnel or equipment.

These practical considerations, along with the time and expense required to install and calibrate the flight instrumentation, are so significant that it is common to fly aircraft operationally without air flow angle instrumentation, despite the known importance of air flow angles for piloting, flight control, flight dynamics, aircraft performance, and safety. Airspeed sensing has the same general problems as air flow angle sensing, but the impact on airspeed accuracy is much smaller, because the airspeed involves the generally large magnitude of the air-relative velocity, whereas the air flow angles involve relatively small components of the air-relative velocity vector. Airspeed is essential for flight operations and safety, so that nearly all aircraft have calibrated sensors for airspeed.

Many approaches have been studied to estimate air flow angles without direct sensing, including kinematic reconstruction [4-7], Kalman filtering [8-11], model-based estimation [12], complementary filtering [13], local pressure measurement processing [14,15], and neural networks [16-18]. However, these approaches can involve complex and expensive calibration, complicated post-flight calculations, control surface deflection measurements, analyst selection of tuning parameter values, and generally high complexity and expense.

This work describes and demonstrates a novel real-time algorithm that accurately estimates air flow angles using only Inertial Measurement Unit (IMU) sensor data, Global Positioning System (GPS) data, PX4 software, and the computing capability available on small, lightweight, and inexpensive Pixhawk Cube Orange hardware. Figure 2 shows the Pixhawk Cube Orange, along with size, weight, and cost information. The air flow angle estimation algorithm is simple enough to execute in real time at 50 Hz using the sensor data and computing capability available on a Pixhawk Cube Orange. The approach can also be extended to operate over large ranges of angle of attack and flank angle.

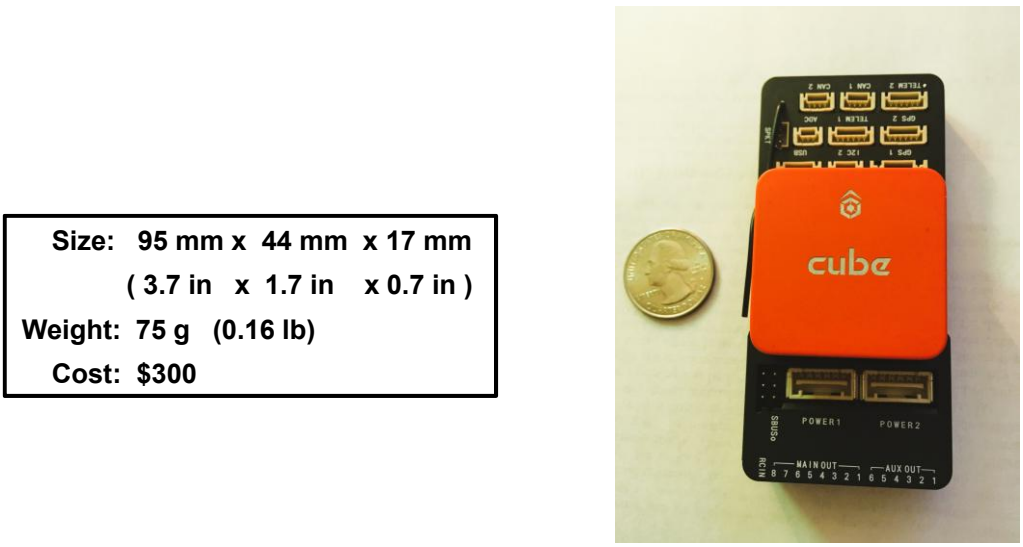


Figure 2. Pixhawk Cube Orange

An F-16 nonlinear simulation with realistic sensor models was used to develop and demonstrate the approach. Flight tests were conducted on a fixed-wing general aviation aircraft equipped with calibrated air flow angle vane sensors mounted on the wing and a Pixhawk Cube Orange mounted inside the fuselage near the aircraft center of gravity. This was done to demonstrate and validate the real-time air flow angle estimation algorithm in flight using a small commercial off-the-shelf (COTS) flight controller onboard the aircraft, and to quantify the practical accuracy.

Section II describes the algorithm developed for onboard real-time estimation of air flow angle data using a Pixhawk Cube Orange, along with the piloted flight test maneuvers and the in-flight calibration procedure. Section III describes the F-16 nonlinear simulation and the Cirrus SR-22 flight test aircraft used in this work. This section also includes information on a subscale aircraft called SEARCH-1, which was used for developmental flight testing. Application results for the real-time air flow angle estimation algorithm are presented in Section IV. In subsection IV.A, the algorithm is demonstrated using an F-16 nonlinear simulation with realistic sensor models and measurement noise. Flight test results using a Cirrus SR-22 fixed-wing general aviation aircraft are shown in subsection IV.B. The algorithm was implemented on a Pixhawk Cube Orange installed inside the fuselage of the SR-22 aircraft with calibrated air flow angle vane sensors mounted on a wing boom. Air flow angle estimates from the algorithm running in real time onboard the aircraft are compared to flight data from the calibrated air flow vane sensors mounted on the wing. Novel aspects of the approach developed and described in this work are presented in Section V, along with practical and computational considerations. Section VI contains a summary and conclusions.

All of the air flow angle estimation algorithm development, flight simulation, data analysis, and modeling tasks for this work were done using routines from a system identification software toolbox written in MATLAB®, called System IDentification Programs for AirCraft, or SIDPAC [1,19]. The SIDPAC software toolbox was developed at NASA Langley and has been applied successfully to a wide variety of wind tunnel and flight test experiments [1,20-22].

II. Method

The general idea behind the real-time air flow angle estimation algorithm is that for an aircraft in flight, the effects of the angle of attack and flank angle are dominant in the aerodynamic forces along the vertical and lateral body-axis translational degrees of freedom, respectively. This is evidenced by the common experience of a passenger or pilot feeling sudden and varied motions during flight in turbulence, as the result of dynamic changes in the air flow angles.

Translational accelerometers mounted in alignment with the aircraft body axes measure the acceleration due to specific applied forces in those directions [1,2]. Assuming that the line of action of the thrust is along the x body axis of the aircraft, translational accelerometers mounted in alignment with the z and y body axes measure acceleration due to applied forces that are purely aerodynamic.

®MATLAB and Simulink are a registered trademarks of The MathWorks, Inc. In this work, the simpler forms MATLAB and Simulink are used for MATLAB® and Simulink®, respectively.

Figure 3 shows a flow chart for the real-time air flow angle estimation algorithm. The next sections discuss and explain the component parts of this flow chart in detail.

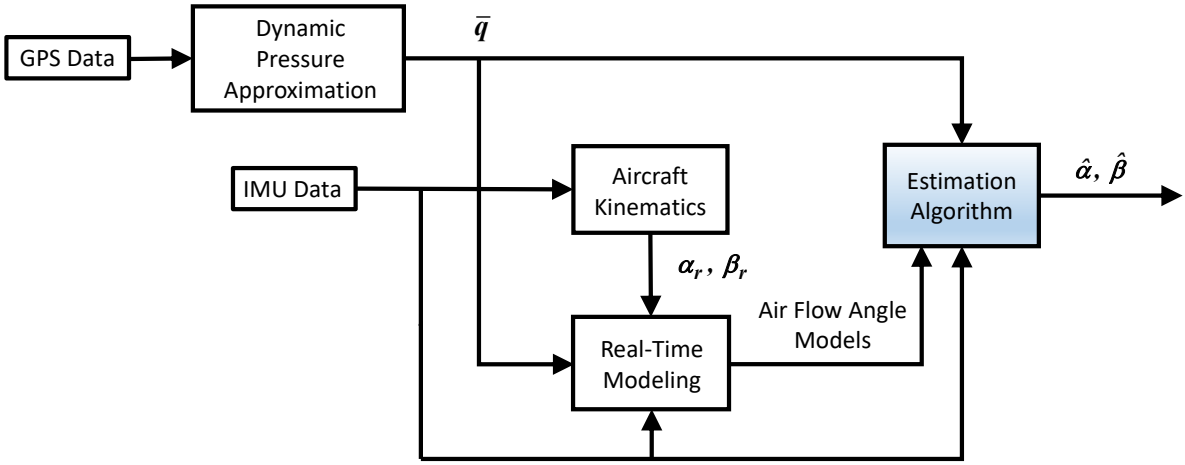


Figure 3. Air flow angle estimation high-level flowchart

A. Air Flow Angle Models

For a fixed-wing aircraft in flight at low nominal angles of attack (away from stall), the aerodynamics in the vertical and lateral body-axis directions can be accurately characterized using linear models.

1. Vertical Body-Axis Aerodynamic Force Model

The vertical body-axis aerodynamic force can be characterized using the linear model

$$Z = mga_z = Z_\alpha \alpha + Z_q q + Z_{\delta_e}\delta_e + Z_o \tag{1}$$

Note that the linear model parameters $Z_\alpha, Z_q, Z_{\delta_e}, Z_o$ are not the same as those typically used in aircraft stability and control analysis [1,2]. Use of Eq. (1) typically would require measurements of the control surface deflection δ_e. To remove the dependence on control surface deflection δ_e, and thereby avoid the need for control surface deflection measurements, note that the linearized pitching moment equation of motion is [1]

$$\dot{q} = M_\alpha \alpha + M_q q + M_{\delta_e}\delta_e + M_o \tag{2}$$

Equation (2) can be arranged to express the control surface deflection δ_e in terms of constants, pitch rate, pitch rate derivative, and angle of attack,

$$\delta_e = \frac{1}{M_{\delta_e}}\left(\dot{q} - M_\alpha \alpha - M_q q - M_o\right) \tag{3}$$

Combining Eqs. (1) and (3),

$$mga_z = \left(Z_\alpha - Z_{\delta_e} \frac{M_\alpha}{M_{\delta_e}} \right) \alpha + \left(Z_q - Z_{\delta_e} \frac{M_q}{M_{\delta_e}} \right) q + \frac{Z_{\delta_e}}{M_{\delta_e}} \dot{q} + \left(Z_o - Z_{\delta_e} \frac{M_o}{M_{\delta_e}} \right) \tag{4}$$

Aerodynamic vertical force and pitching moment depend linearly on dynamic pressure [1],

$$Z = \bar{q} S C_Z \qquad M = \bar{q} S \bar{c} C_m \tag{5}$$

It follows that all of the vertical force and pitching moment parameters on the right sides of Eqs. (1) and (2) also depend linearly on dynamic pressure. Using the definitions

$$Z_\alpha = \bar{q} S C_{Z_\alpha} \qquad Z_q = \bar{q} S C_{Z_q} \frac{\bar{c}}{2V_o} \qquad Z_{\delta_e} = \bar{q} S C_{Z_{\delta_e}} \qquad Z_o = \bar{q} S C_{Z_o} \tag{6}$$

$$M_\alpha = \frac{\bar{q} S \bar{c}}{I_y} C_{m_\alpha} \qquad M_q = \frac{\bar{q} S \bar{c}}{I_y} C_{m_q} \frac{\bar{c}}{2V_o} \qquad M_{\delta_e} = \frac{\bar{q} S \bar{c}}{I_y} C_{m_{\delta_e}} \qquad M_o = \frac{\bar{q} S \bar{c}}{I_y} C_{m_o} \tag{7}$$

Eq. (4) can be modified to

$$\frac{g a_z}{\bar{q}} = a_1 \alpha + a_2 q + a_3 \frac{\dot{q}}{\bar{q}} + a_0 \tag{8}$$

where

$$a_1 = \frac{S}{m} \left(C_{Z_\alpha} - C_{Z_{\delta_e}} \frac{C_{m_\alpha}}{C_{m_{\delta_e}}} \right) \tag{9a}$$

$$a_2 = \frac{S \bar{c}}{m 2V_o} \left(C_{Z_q} - C_{Z_{\delta_e}} \frac{C_{m_q}}{C_{m_{\delta_e}}} \right) \tag{9b}$$

$$a_3 = \frac{I_y}{m \bar{c}} \left(\frac{C_{Z_{\delta_e}}}{C_{m_{\delta_e}}} \right) \tag{9c}$$

$$a_0 = \frac{S}{m} \left(C_{Z_o} - C_{Z_{\delta_e}} \frac{C_{m_o}}{C_{m_{\delta_e}}} \right) \tag{9d}$$

Equation (8) is the air flow model for angle of attack. The unknown model parameters to be determined during in-flight calibration are $a_1, a_2, a_3, a_0,$ defined in Eqs. (9a)-(9d). Because

these definitions include nondimensional stability and control derivatives (e.g., $C_{m_{\delta_e}}$), the air flow model parameters a_1, a_2, a_3, a_0 depend on aircraft configuration (e.g., flaps up, gear up) and flight condition, as well as aircraft mass/inertia properties and wing geometry.

For this work, the aircraft configuration, mass/inertia properties, and wing geometry are assumed to be constant. In addition, flight condition changes are assumed to be moderate, so that the stability and control derivatives can be assumed constant. These are good assumptions for typical operational air flow angles and flight conditions. All of these assumptions could be removed or relaxed by implementing a more complex aerodynamic model and calibrating the model for different fuel states, loading, and aircraft configurations.

2. Lateral Body-Axis Aerodynamic Force Model

The development of the lateral body-axis aerodynamic force model is analogous to the preceding development for vertical body-axis aerodynamic force model. The lateral aerodynamics equations are

$$Y = mga_y = Y_{\beta_f}\beta_f + Y_r r + Y_{\delta_r}\delta_r + Y_o \tag{10}$$

$$\dot{r} = N_{\beta_f}\beta_f + N_r r + N_{\delta_r}\delta_r + N_o \tag{11}$$

$$\delta_r = \frac{1}{N_{\delta_r}}\left(\dot{r} - N_{\beta_f}\beta_f - N_r r - N_o\right) \tag{12}$$

$$mga_y = \left(Y_{\beta_f} - Y_{\delta_r}\frac{N_{\beta_f}}{N_{\delta_r}}\right)\beta_f + \left(Y_r - Y_{\delta_r}\frac{N_r}{N_{\delta_r}}\right)r + \frac{Y_{\delta_r}}{N_{\delta_r}}\dot{r} + \left(Y_o - Y_{\delta_r}\frac{N_o}{N_{\delta_r}}\right) \tag{13}$$

Using the definitions

$$Y = \bar{q}SC_Y \qquad N = \bar{q}SbC_n \tag{14}$$

$$Y_{\beta_f} = \bar{q}SC_{Y_{\beta_f}} \qquad Y_r = \bar{q}SC_{Y_r}\frac{b}{2V_o} \qquad Y_{\delta_r} = \bar{q}SC_{Y_{\delta_r}} \qquad Y_o = \bar{q}SC_{Y_o} \tag{15}$$

$$N_{\beta_f} = \frac{\bar{q}Sb}{\Gamma}\left(I_{xz}C_{l_{\beta_f}} + I_x C_{n_{\beta_f}}\right) \qquad N_r = \frac{\bar{q}Sb}{\Gamma}\left(I_{xz}C_{l_r} + I_x C_{n_r}\right)\frac{b}{2V_o}$$

$$N_{\delta_r} = \frac{\bar{q}Sb}{\Gamma}\left(I_{xz}C_{l_{\delta_r}} + I_x C_{n_{\delta_r}}\right) \qquad N_o = \frac{\bar{q}Sb}{\Gamma}\left(I_{xz}C_{l_o} + I_x C_{n_o}\right) \tag{16a}$$

$$C'_{n_{\beta_f}} = \frac{1}{\Gamma}\left(I_{xz}C_{l_{\beta_f}} + I_x C_{n_{\beta_f}}\right) \qquad C'_{n_r} = \frac{1}{\Gamma}\left(I_{xz}C_{l_r} + I_x C_{n_r}\right)$$
$$C'_{n_{\delta_r}} = \frac{1}{\Gamma}\left(I_{xz}C_{l_{\delta_r}} + I_x C_{n_{\delta_r}}\right) \qquad C'_{n_o} = \frac{1}{\Gamma}\left(I_{xz}C_{l_o} + I_x C_{n_o}\right) \tag{16b}$$

$$\Gamma = I_x I_z - I_{xz}^2 \tag{16c}$$

Eq. (13) can be modified to

$$\frac{g a_y}{\bar{q}} = b_1 \beta_f + b_2 r + b_3 \frac{\dot{r}}{\bar{q}} + b_0 \tag{17}$$

where

$$b_1 = \frac{S}{m}\left(C_{Y_{\beta_f}} - C_{Y_{\delta_r}} \frac{C'_{n_{\beta_f}}}{C'_{n_{\delta_r}}}\right) \tag{18a}$$

$$b_2 = \frac{Sb}{m2V_o}\left(C_{Y_r} - C_{Y_{\delta_r}} \frac{C'_{n_r}}{C'_{n_{\delta_r}}}\right) \tag{18b}$$

$$b_3 = \frac{1}{mb}\left(\frac{C_{Y_{\delta_r}}}{C'_{n_{\delta_r}}}\right) \tag{18c}$$

$$b_0 = \frac{S}{m}\left(C_{Y_o} - C_{Y_{\delta_r}} \frac{C'_{n_o}}{C'_{n_{\delta_r}}}\right) \tag{18d}$$

The same caveats stated earlier concerning the validity of the vertical aerodynamic force model also apply to the lateral aerodynamic force model. The more complicated expressions in Eqs. (16a)-(16c) result from the presence of the product of inertia I_{xz}, which couples the yawing moment and rolling moment aerodynamics [1,2].

The flank angle is related to the sideslip angle by [1,2]

$$\beta_f = \tan^{-1}\left(\frac{\tan\beta}{\cos\alpha}\right) \tag{19}$$

For small angles of attack, $\beta_f \approx \beta$. The vane sensor measures flank angle, so the flank angle was used throughout this work.

Equations (8) and (17) are linear equations relating accelerometer data, air flow angle data, angular rate data, angular acceleration data, and dynamic pressure data. Under the conditions explained earlier, the model parameters a_1, a_2, a_3, a_0 in Eq. (8) and b_1, b_2, b_3, b_0 in Eq. (17) can be considered unknown constants to be determined during the in-flight model calibration.

B. Air Flow Angle Estimation

If the model parameters in Eqs. (8) and (17) are known, and real-time data are available for translational accelerations, angular rates, angular accelerations, and dynamic pressure, then the model equations can be inverted to produce expressions for air flow angle estimates $\hat{\alpha}$ and $\hat{\beta}_f$. The resulting equations are

$$\hat{\alpha} = \frac{1}{a_1}\left(\frac{g a_z}{\bar{q}} - a_2 q - a_3 \frac{\dot{q}}{\bar{q}} - a_0 \right) \tag{20}$$

$$\hat{\beta}_f = \frac{1}{b_1}\left(\frac{g a_y}{\bar{q}} - b_2 r - b_3 \frac{\dot{r}}{\bar{q}} - b_0 \right) \tag{21}$$

The Pixhawk Cube Orange sensors include gyroscopes to measure angular rates and accelerometers to measure translational accelerations excluding gravity. The processes for obtaining real-time data for dynamic pressure and angular acceleration will be explained in the next two subsections.

An in-flight real-time model calibration process was used to find accurate values for the model parameters a_1, a_2, a_3, a_0 in Eq. (20) and b_1, b_2, b_3, b_0 in Eq. (21). The in-flight model calibration process uses kinematic reconstruction and real-time modeling methods applied to flight data from piloted calibration maneuvers. These topics will be explained later.

The in-flight model calibration process is executed in real time onboard the aircraft by the Pixhawk Cube Orange in calibration mode using Eqs. (8) and (17). Then the Pixhawk Cube Orange is switched manually to estimation mode, where Eqs. (20) and (21) are executed in real time using flight data with model parameter values obtained from the in-flight model calibration.

C. Dynamic Pressure

For subsonic flight, dynamic pressure can be computed from measurements of airspeed V, ambient temperature T_a, and ambient pressure P_a,

$$\rho = P_a / \left(R T_a \right) \tag{22}$$

$$\bar{q} = \frac{1}{2} \rho V^2 \tag{23}$$

The Pixhawk Cube Orange has sensors for ambient temperature and pressure, but those sensors are inside the device, which is mounted inside the aircraft, so that the temperature and pressure measurements are not accurate for outside air. Assuming that there is not a dedicated

dynamic pressure sensor installed on the aircraft, a rough approximation for dynamic pressure can be obtained using GPS ground speed and GPS altitude from the Pixhawk Cube Orange, with standard atmosphere data or day-of-flight aviation weather information. Of course, using a rough approximation for dynamic pressure will adversely impact the real-time air flow angle estimates.

Alternatively, if dynamic pressure can be obtained by direct measurement, e.g., using a pitot tube installed on the aircraft and a calibrated pressure transducer, the Pixhawk Cube Orange can do the analog-to-digital (A/D) conversion or read digital data in real time. In that case, GPS data are not needed for the air flow angle estimation algorithm, and the flow chart in Fig. 3 can be modified as shown in Fig. 4.

An important point is that GPS data are only used in the air flow angle estimation algorithm to obtain an estimate for dynamic pressure. If instead the dynamic pressure can be measured, then the air flow angle estimation algorithm works without GPS data, which is a significant practical advantage in environments where GPS is unavailable, unreliable, or actively denied.

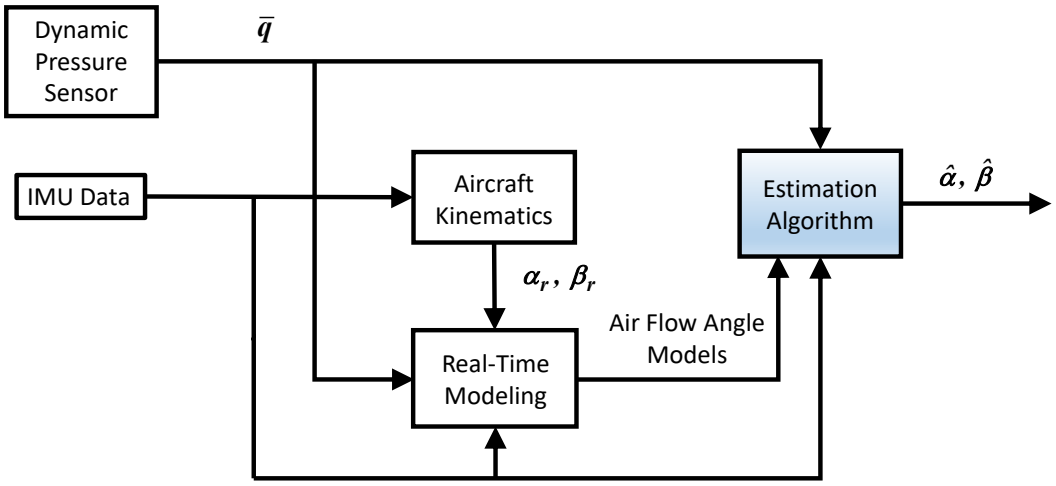


Figure 4. Air flow angle estimation high-level flowchart without GPS data

D. Real-Time Data Smoothing and Differentiation

The flight data from the Pixhawk Cube Orange was very consistent but slightly noisier compared to data collected from Garmin G600® instrumentation installed on the SR-22 aircraft. The Garmin G600 instrumentation was approximately 100 times more expensive to acquire and install on the aircraft compared to the Pixhawk Cube Orange. Figure 5 shows an example comparison of pitch rate measurements. The root-mean-square (RMS) noise level for the pitch rate data from the Garmin G600 was 0.07 deg/s, compared to 0.26 deg/s for the pitch rate data from the Pixhawk Cube Orange. These noise levels were determined directly from the measured flight data, using an optimal Fourier smoothing technique [1,19].

®Garmin and G600 are registered trademarks of Garmin, Inc. and its subsidiaries. In this work, the simpler form Garmin G600 is used for Garmin G600®.

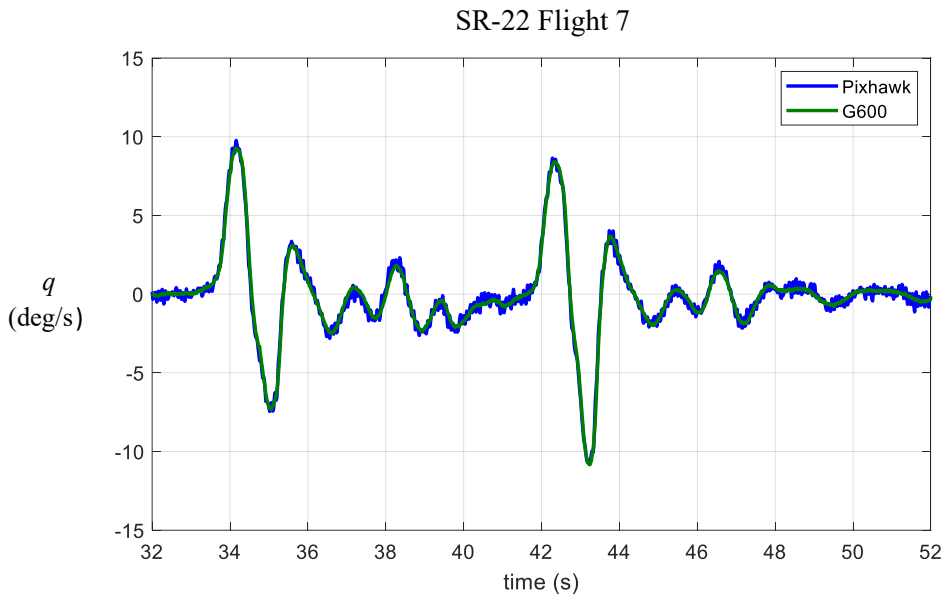


Figure 5. Comparison of pitch rate measurements on the SR-22 aircraft in flight

To mitigate the effects of sensor noise, a real-time data smoothing process was implemented on the Pixhawk Cube Orange. This data smoothing incurred a time delay of 2 samples at 50 Hz or 0.04 s, as will be explained next.

The real-time data smoothing was done using a sliding local 2nd-order smoothing polynomial. Example local results are shown in Fig. 6. Fixed smoothing weights determined from local least-squares modeling were applied to the real-time data to obtain a local smoothing polynomial, from which a smoothed value and smoothed time derivative were extracted at the center point of the local polynomial fit [1]. Using future data relative to the smoothed and differentiated data point implements very effective data smoothing and smooth numerical differentiation.

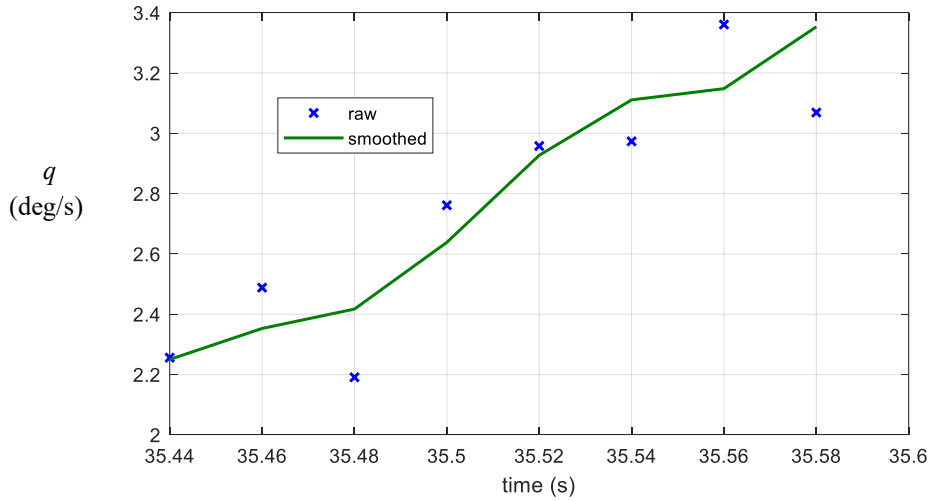


Figure 6. Local polynomial data smoothing

The sliding local 2nd-order smoothing polynomial fit applied in this work used measured data from 2 adjacent sampling times both before and after the center point, in addition to the measured data at the center point where the smoothed value and smoothed derivative value were calculated, for a total of 5 local measured data points. This implements a real-time low-pass filter with cutoff frequency at approximately 5 Hz. The local data smoothing and smooth differentiation are zero-lag processes, but are computed at a center point located 2 sample times behind the current real time, resulting in a delay of exactly 2 sample times. This time delay was 0.04 s for 2 sampling intervals at the 50 Hz data sampling rate used in this work. Real-time data smoothing is critical for effective noise rejection, which significantly improves both the in-flight model calibrations and the air flow angle estimation results. Although the time delay incurred to smooth the measured data in real time is detrimental for feedback control and aircraft system identification, the time lag is constant and known, and can therefore be corrected.

The top plot in Fig. 7 shows raw pitch rate measurements from the IMU onboard the Pixhawk Cube Orange, along with smoothed values. The raw data were lagged by 2 samples, to make the comparison valid. The middle plot shows the difference between the raw data and the smoothed data, which is the noise rejected by the data smoothing. The bottom plot shows the smoothed time derivative of the pitch rate data.

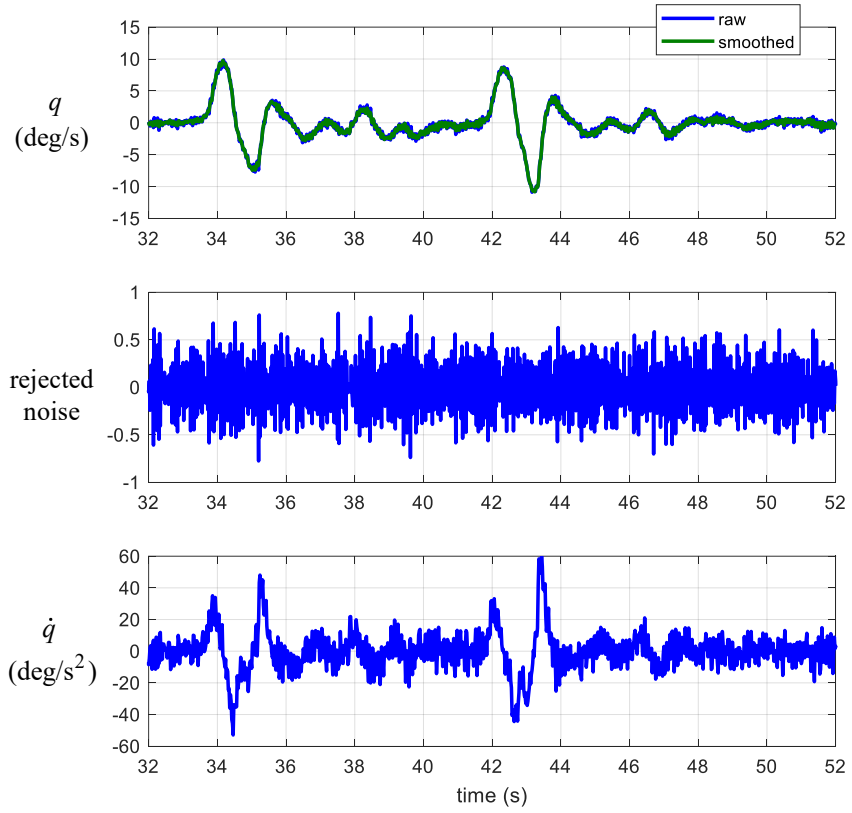


Figure 7. Real-time pitch rate measurements, smoothing, and smoothed time derivative

Figure 8 shows analogous data for yaw rate measurements, which were generally less noisy than the pitch rate measurements. The RMS noise level for the yaw rate data from the Garmin 600 was 0.05 deg/s, compared to 0.06 deg/s for the Pixhawk Cube Orange data shown in Fig. 8. This data suggests that the mounting fabricated for the Pixhawk Cube Orange may have had flexibility in pitch, so that a sturdier mount might reduce the pitch rate RMS noise level of the Pixhawk Cube Orange sensor data to nearly the same low noise level observed for the more expensive Garmin 600 sensor data.

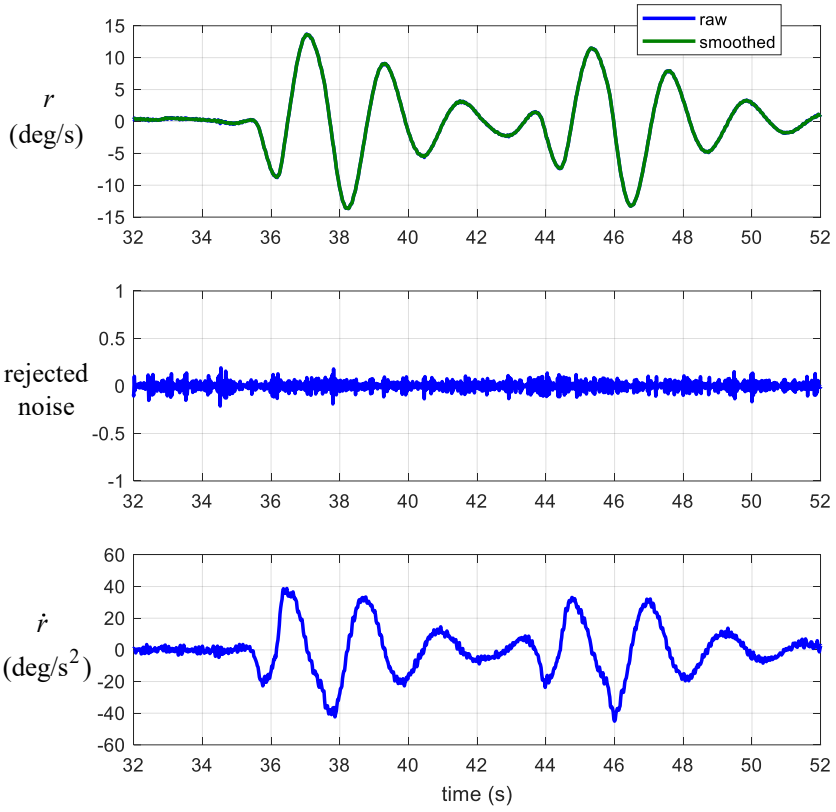


Figure 8. Real-time yaw rate measurements, smoothing, and smoothed time derivative

E. Kinematic Reconstruction

The model parameters in Eqs. (8) and (17) were determined during in-flight calibration. To do this, data for the angle of attack and flank angle are required. However, because the algorithm is intended to replace flight instrumentation for these air flow angles, the air flow angle information for in-flight model calibration must be obtained in another way. This can be done by reconstructing angle of attack and flank angle data in real time using other sensor data during a dynamic flight test maneuver in relatively calm air.

For flight at low air flow angles with no wind, the angle of attack and flank angle can be reconstructed using the following coupled, nonlinear differential equations [23]:

$$\dot{\alpha}_r = q - p\beta_{f_r} + \frac{g}{V}\left(\cos\theta\cos\phi + \Delta a_z\right) \tag{24}$$

$$\dot{\beta}_{f_r} = p\alpha_r - r + \frac{g}{V}\left(\cos\theta\sin\phi + \Delta a_y\right) \tag{25}$$

The Pixhawk Cube Orange provided real-time data for translational accelerations $\left(a_y, a_z\right)$, angular rates $\left(p,q,r\right)$, Euler angles $\left(\theta,\phi\right)$, and GPS ground speed, which was used to approximate airspeed V, as discussed earlier.

Because computing air flow angle data from Eqs. (24) and (25) involves time integration, the accelerometer measurements must be perturbation quantities. The initial flight condition for the model calibration flight test maneuver is steady trimmed wings-level flight at constant altitude, so that the initial value a_{z_o} can be found as

$$a_{z_o} = \bar{a}_z \tag{26a}$$

where 1 s of 50 Hz data at the initial steady trim condition was used to compute the mean value $\bar{a}_z$. Then the perturbation quantity Δa_z is computed as

$$\Delta a_z = a_z - a_{z_o} \tag{26b}$$

A similar approach was used to determine Δa_y.

Initial conditions for the air flow angle data reconstruction using Eqs. (24) and (25) were obtained by starting the dynamic calibration maneuver from steady, symmetric, wings-level flight at constant altitude. In that flight condition,

$$\alpha_r\left(0\right) = \bar{\theta} \qquad \text{or} \qquad \alpha_r\left(0\right) = \sin^{-1}\left(\bar{a}_x\right) \tag{27}$$

$$\beta_{f_r}\left(0\right) = 0 \tag{28}$$

Mean values used for initializing the angle of attack reconstruction were based on 1 s of 50 Hz data at the initial steady trim condition. Using $\bar{\theta}$ or $\sin^{-1}(\bar{a}_x)$ for the angle of attack initial condition was found to be nearly equivalent, but the initial condition for angle of attack was set using $\bar{\theta}$, because the calculation is simpler. Second-order Runge-Kutta integration [1] was applied on the Pixhawk Cube Orange to solve Eqs. (24) and (25) in real time.

Despite the steady initial condition, the angular rate and accelerometer sensor data still typically have bias errors, but not scale factor errors [1]. The PX4 software running on the Pixhawk Cube Orange has the capability to estimate time-varying and temperature-dependent biases in real time, so that long-term effects of these instrumentation errors can be mostly removed. However, in practice, there are remaining small bias errors in the short term, which cause the air flow angle data reconstructed using Eqs. (24) and (25) to drift with time, due to time integration of small constant bias errors in the angular rate and accelerometer sensor measurements. This drift will be accounted for and removed during the real-time air flow angle model calibration process described in the next subsection.

Real-time air flow angle data reconstruction was implemented by numerically solving Eqs. (24) and (25) on the Pixhawk Cube Orange in calibration mode. Piloted flight test maneuvers for the in-flight calibration were pitch-yaw doublet sequences. Other piloted flight test maneuvers were flown as well, and it was found that these dynamic maneuvers could also be used for the in-flight calibration. However, the piloted pitch-yaw doublet sequence was the simplest and produced good results.

During flight testing, it was found that the air flow angle reconstruction did not require strictly calm air to work adequately because the effects of light and inconsistent wind were mostly removed by the time integration and the real-time least-squares modeling described in the next subsection.

Figure 9 shows real-time angle of attack and flank angle data reconstructions for an in-flight calibration pitch-yaw doublet maneuver. The drift due to sensor biases can be easily seen. Note that the noise levels for the reconstructed air flow angles are very low, due to the real-time data smoothing and the integration of Eqs. (24) and (25), which effectively smoothed the remaining noise on the translational acceleration and angular rate inputs.

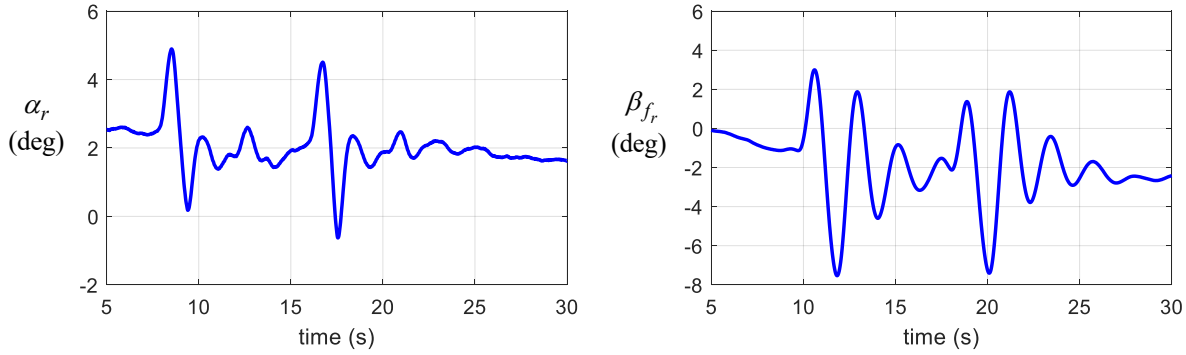


Figure 9. Real-time air flow angle data reconstructions

F. Real-Time Air Flow Angle Model Calibration

The air flow angle model equations (8) and (17) are linear regression models, with model terms (also called regressors) on the right side and the dependent variable on the left side. Determining the values of the unknown model parameters in these equations in real time constitutes the in-flight calibration of the air flow angle models.

Consider the vertical aerodynamic force model

$$\frac{g\Delta a_z}{\bar{q}} = a_1\alpha_r + a_2 q + a_3\frac{\dot{q}}{\bar{q}} + a_4 t + a_0 \tag{29}$$

Compared to Eq. (8), Eq. (29) uses the perturbation quantity Δa_z, reconstructed angle of attack α_r, and includes time t as a model term. These changes will be explained in the following development.

The modeling based on Eq. (29) for N data points can be formulated as a standard least-squares regression problem as follows:

$$\boldsymbol{z} = \boldsymbol{X\theta} + \boldsymbol{\varepsilon} \tag{30}$$

where

$$\boldsymbol{z} = g\left[\Delta a_z(1)/\bar{q}(1) \quad \Delta a_z(2)/\bar{q}(2) \quad \ldots \quad \Delta a_z(N)/\bar{q}(N)\right]^T \tag{31a}$$

$$\boldsymbol{X} = \begin{bmatrix} \alpha_r(1) & q(1) & \dot{q}(1)/\bar{q}(1) & 0 & 1 \\ \alpha_r(2) & q(2) & \dot{q}(1)/\bar{q}(2) & \Delta t & 1 \\ \vdots & \vdots & \vdots & \vdots & \vdots \\ \alpha_r(N) & q(N) & \dot{q}(1)/\bar{q}(N) & (N-1)\Delta t & 1 \end{bmatrix} \tag{31b}$$

$$\boldsymbol{\theta} = \begin{bmatrix} a_1 & a_2 & a_3 & a_4 & a_0 \end{bmatrix}^T \tag{31c}$$

$$\boldsymbol{\varepsilon} = \begin{bmatrix} \varepsilon(1) & \varepsilon(2) & \ldots & \varepsilon(N) \end{bmatrix}^T = N\times 1 \text{ vector of equation errors} \tag{31d}$$

This is an over-determined set of equations for the unknown model parameters a_1, a_2, a_3, a_4, a_0 in vector $\boldsymbol{\theta}$, which can be solved using standard least-squares techniques.

The best estimate of $\boldsymbol{\theta}$ in a least-squares sense comes from minimizing the sum of squared differences between the dependent variable measurements $\boldsymbol{z}$ and the model output $\boldsymbol{y} = \boldsymbol{X\theta}$,

$$J(\boldsymbol{\theta}) = \frac{1}{2}(\boldsymbol{z} - \boldsymbol{X\theta})^T(\boldsymbol{z} - \boldsymbol{X\theta}) \tag{32}$$

The least-squares solution for the unknown parameter vector $\boldsymbol{\theta}$ is [1]

$$\hat{\boldsymbol{\theta}} = \left(\boldsymbol{X}^T \boldsymbol{X} \right)^{-1} \boldsymbol{X}^T \boldsymbol{z} \tag{33}$$

Including a time vector regressor in a model like Eq. (29) effectively removes the effect of a linear drift with time in any of the other regressors. The same statement applies for the constant model term, also called the bias. To see this, assume that α_r has both a bias and a linear drift with time in addition to dynamic information $\Delta\alpha_r$, so that Eq. (29) is

$$\frac{g\Delta a_z}{\bar{q}} = a_1 \left(\Delta\alpha_r + \alpha_{r_t} t + \alpha_{r_o} \right) + a_2 q + a_3 \frac{\dot{q}}{\bar{q}} + a_4 t + a_0 \tag{34}$$

Collecting terms,

$$\frac{g\Delta a_z}{\bar{q}} = a_1 \Delta\alpha_r + a_2 q + a_3 \frac{\dot{q}}{\bar{q}} + \left(\alpha_{r_t} + a_4 \right) t + \left(\alpha_{r_o} + a_0 \right) \tag{35}$$

Including the regressor *t* removes the linear drift with time from the reconstructed angle of attack, which occurs due to the time integration using angular rate and accelerometer data with bias errors, cf. Fig. 9. When the algorithm is in estimation mode, the model is inverted to estimate angle of attack, cf. Eq. (20), but the model term accounting for linear drift with time is discarded because that model term was used only to remove the linear drift with time in the angle of attack reconstruction. Omitting the drift term in the estimation equation produces an angle of attack estimate without a linear drift with time, which is the desired result.

Considering that q, $\dot{q}$, and Δa_z will have very small biases for a calibration maneuver starting from steady symmetric wings-level flight at constant altitude, the bias term in the model will account for only the offset in reconstructed angle of attack, which is correct at the start of the calibration maneuver because of the well-defined starting condition. The bias parameter cannot be discarded from the estimation equation because that parameter carries the information for the steady value of angle of attack. Accordingly, the calibration model is only accurate for a range of angle of attack where the calibration model is linear relative to the initial reference flight condition for the calibration maneuver. However, this limitation could be overcome by repeating the calibration at different reference flight conditions or by using a more complex model structure.

Using the angle of attack model parameters determined from Eqs. (31) and (33) when the algorithm is in calibration mode, the angle of attack estimation equation (20) applied in estimation mode becomes

$$\hat{\alpha} = \frac{1}{\hat{a}_1} \left(\frac{g\Delta a_z}{\bar{q}} - \hat{a}_2 q - \hat{a}_3 \frac{\dot{q}}{\bar{q}} - \hat{a}_0 \right) \tag{36}$$

An analogous development for the lateral aerodynamic force model results in

$$\frac{g\Delta a_y}{\bar{q}} = b_1\beta_{f_r} + b_2 r + b_3\frac{\dot{r}}{\bar{q}} + b_4 t + b_0 \tag{37}$$

with the associated flank angle estimation equation

$$\hat{\beta}_f = \frac{1}{\hat{b}_1}\left(\frac{g\Delta a_y}{\bar{q}} - \hat{b}_2 r - \hat{b}_3\frac{\dot{r}}{\bar{q}} - \hat{b}_0\right) \tag{38}$$

Equation (33) provides a batch least-squares estimate of the unknown model parameters. This calculation can be made recursive, so that the time evolution of the model parameter estimates can be examined. In addition, the calibration model parameter estimates are calculated and available continuously in time, instead of producing a single batch estimate $\hat{\boldsymbol{\theta}}$ after all of the calibration maneuver data have been collected.

The recursive version of Eq. (33) is [1]

$$\hat{\boldsymbol{\theta}}(n+1) = \hat{\boldsymbol{\theta}}(n) + \boldsymbol{K}(n+1)\left[z(n+1) - \boldsymbol{x}^T(n+1)\hat{\boldsymbol{\theta}}(n)\right] \tag{39}$$

$$\boldsymbol{K}(n+1) = \boldsymbol{\mathcal{D}}(n)\boldsymbol{x}(n+1)\left[1 + \boldsymbol{x}^T(n+1)\boldsymbol{\mathcal{D}}(n)\boldsymbol{x}(n+1)\right]^{-1} \tag{40}$$

$$\boldsymbol{\mathcal{D}}(n+1) = \boldsymbol{\mathcal{D}}(n) - \boldsymbol{\mathcal{D}}(n)\boldsymbol{x}(n+1)\left[1 + \boldsymbol{x}^T(n+1)\boldsymbol{\mathcal{D}}(n)\boldsymbol{x}(n+1)\right]^{-1}\boldsymbol{x}^T(n+1)\boldsymbol{\mathcal{D}}(n) \tag{41}$$

where n is the sample time index, $\boldsymbol{x}(n)$ is the nth row of the $\boldsymbol{X}$ matrix, and $z(n)$ is the nth element of the $\boldsymbol{z}$ vector, cf. Eqs. (31a)-(31b).

The initial conditions are

$$\begin{aligned}\hat{\boldsymbol{\theta}}(0) &= \mathbf{0} \\ \boldsymbol{\mathcal{D}}(0) &= 10^8\mathbf{I}\end{aligned} \tag{42}$$

which represents having no prior knowledge about the model parameters. Because the recursive parameter estimation is a reformulation of the batch parameter estimation, the parameter estimates from both calculations will be the same after the last data point is processed.

The recursive least-squares parameter estimation in Eqs. (39)-(42) was implemented and applied in this work for the real-time in-flight air flow angle model calibrations.

G. Summary

A summary of the steps required to first calibrate then apply the models to estimate air flow angles is presented below.

1. Real-Time In-Flight Calibration

a) Starting in steady symmetric wings-level flight at constant altitude, the Pixhawk Cube Orange is switched manually into calibration mode, then the pilot executes a pitch-yaw doublet sequence twice. Note that other dynamic maneuvers could be used, but the pitch-yaw doublet sequence is simple, works well, and is efficient.

b) Air flow angle data used for the real-time modeling is computed from real-time kinematic reconstruction using Eqs. (24)-(28). Bias and drift errors are incurred when reconstructing the air flow angle data, but these errors are removed in the real-time modeling.

c) Dynamic pressure data is estimated from GPS altitude and GPS ground speed using Eqs. (22) and (23). Alternatively, dynamic pressure data can come from a dynamic pressure sensor measurement input to the Pixhawk Cube Orange.

d) Flight data for angular rates, translational acceleration, and dynamic pressure are smoothed in real-time using a local polynomial smoothing technique described in section II.D. and Ref. [1]. The same approach is used to provide smoothed angular acceleration data from angular rate data.

e) Unknown parameters a_1, a_2, a_3, a_4, a_0 in Eq. (29) and b_1, b_2, b_3, b_4, b_0 in Eq. (37) are estimated from flight data in real time using recursive least squares parameter estimation implemented by Eqs. (39)-(42).

2. Real-Time Air Flow Angle Estimation

a) The Pixhawk Cube Orange is switched manually into estimation mode.

b) Angle of attack and flank angle are estimated using Eqs. (36) and (38), respectively, with model parameter estimates from the in-flight calibration procedure. The same real-time data smoothing described in section II.D and Ref. [1] is applied to the real-time flight data for angular rates, translational acceleration, dynamic pressure, and angular acceleration.

All sensing, data processing, data recording, and calculations were done by the Pixhawk Cube Orange onboard the aircraft in real time at 50 Hz.

III. Aircraft

A. F-16 Nonlinear Simulation

The F-16 is a single-seat, multi-role fighter aircraft with a blended wing / body and a cropped delta wing planform with leading edge sweep of 40 deg. Thrust is provided by one General Electric F110-GE-100 or Pratt & Whitney F100-PW-220 afterburning turbofan engine mounted in the rear fuselage. Figure 10 is a photograph of the F-16 in flight. Aircraft geometry and nominal mass properties are given in Table 1.

The F-16 nonlinear simulation has controls for throttle δ_{th}, stabilator δ_s, aileron δ_a, and rudder δ_r. Speed brake and flaps were assumed fixed at zero deflection with landing gear retracted.



Figure 10. F-16 Aircraft

Credit: NASA Langley Research Center

Table 1. Aircraft Geometry and Mass Properties

	F-16	SR-22
$\bar{c}$, ft	11.32	4.03
b, ft	30	38.3
S, ft^2	300	144.9
x_{cg}, ft	$0.25\,\bar{c}$	11.93
y_{cg}, ft	0	0
z_{cg}, ft	0	8.08
m, slug	637	106
I_x, slug-ft^2	9,496	1,575
I_y, slug-ft^2	55,814	9,257
I_z, slug-ft^2	63,100	10,465
I_{xz}, slug-ft^2	982	163

Nondimensional aerodynamic force and moment coefficient data were derived from a low-speed static wind-tunnel test and a dynamic forced-oscillation wind-tunnel test, both conducted using a 16% scale model of the F-16. The aerodynamic database applies to the F-16 flown out of ground effect with zero deflection of flaps and speed brake, landing gear retracted, and no external stores, over a wide range of angle of attack and sideslip angle.

The F-16 nonlinear simulation was programmed completely in MATLAB [1,19]. Full nonlinear equations of motion, including turbine engine gyroscopic effects, were used. Complete details on the F-16 nonlinear simulation can be found in Ref. [1], Appendix D.

B. SEARCH-1 Subscale Aircraft

SEARCH-1 is a modified E-Flite Carbon-Z Cessna 150 (CZ-150) subscale aircraft used for developmental flight testing at the CERTAIN flight test range, located at NASA Langley Research Center. Figure 11 shows the aircraft in flight. The CZ-150 has a 6.97 ft wingspan, electric-powered single tractor propeller, and weighs 9.5 lbf. Vane sensors for angle of attack and flank angle were installed on a wingtip boom, visible in Fig. 11. Twenty-seven test flights were conducted using this aircraft to develop the real-time air flow angle estimation algorithm and real-time software implementation, and to investigate useful flight test techniques for in-flight calibration of the air flow angle models. This rapid flight test capability was crucial for risk reduction and practical flight test experience before transitioning to the Cirrus SR-22 general aviation aircraft, described next.



Figure 11. SEARCH-1 Subscale Aircraft

Credit: NASA Langley Research Center

C. Cirrus SR-22 Aircraft

The NASA Langley Cirrus SR-22 aircraft is a 4-seat, low-wing cantilever monoplane with composite construction, fixed tricycle landing gear, 310 horsepower reciprocating engine, and a constant-speed tractor propeller. Figure 12 is a photograph of the SR-22 in flight. Aircraft geometry and nominal mass properties are given in Table 1.

The Pixhawk Cube Orange was mounted near the center of gravity of the aircraft on the fuselage floor, as shown in Fig. 13. Physical specifications for the Pixhawk Cube Orange are given in Table 2. The Pixhawk Cube Orange performed the onboard real-time calculations for both the in-flight calibration and the air flow angle estimation using onboard IMU and GPS sensor data. Switching between calibration and estimation modes of operation was done manually by the flight test engineer using a switch on the side of the Pixhawk Cube Orange, visible in Fig. 13. The data were recorded at 50 Hz in log files on a Secure Digital (SD) card inside the Pixhawk Cube Orange.



Figure 12. SR-22 aircraft

Credit: NASA Langley Research Center

Table 2. Pixhawk Cube Orange Physical Characteristics

weight, lbf	0.161
length, in	3.720
width, in	1.744
height, in	1.188

Figure 14 shows the air flow angle vane sensors mounted on the starboard wing of the SR-22. Data from these calibrated sensors were used for validation and comparison to the angle of attack and flank angle estimates from the real-time algorithm running on the Pixhawk Cube Orange. Air flow angle vane sensor data were collected using analog-to-digital conversion applied to analog voltages produced by potentiometers on the rotation axes of the vanes for angle of attack (left of the boom) and flank angle (below the boom). Dynamic pressure was measured using pressure transducers applied to differential pressure from pressure ports located near the tip of the boom shown in Fig. 14. The vane sensor and dynamic pressure measurements were collected and recorded by the onboard SR-22 flight instrumentation system, separately from the Pixhawk Cube Orange.

Table 3 specifies the locations of the vane sensors, Pixhawk Cube Orange, and nominal center of gravity on the SR-22 aircraft using a [FS, BL, WL] coordinate system with origin at the nose of the aircraft. The sign convention is FS positive aft, BL positive out the right wing, and WL positive up.



Figure 13. Pixhawk Cube Orange installed in the SR-22 aircraft

Credit: NASA Langley Research Center



Figure 14. Air flow vanes on the SR-22 aircraft

Credit: NASA Langley Research Center

Table 3. SR-22 Sensors and Center of Gravity Locations

	β_f vane	α vane	Pixhawk Cube Orange	Center of Gravity
FS, ft	11.00	10.75	13.17	11.93
BL, ft	17.92	17.92	0.00	0.00
WL, ft	7.50	7.50	7.25	8.08

All flight tests were conducted with a research pilot flying all of the maneuvers manually, and a single flight test engineer in the back of the aircraft to act as the flight test conductor and switch modes on the Pixhawk Cube Orange at appropriate times. The flight test engineer also monitored real-time 50 Hz User Datagram Protocol (UDP) data from the SR-22 flight

instrumentation system, which were transmitted to a Hewlett-Packard ZBook Power G10 laptop computer in the back of the aircraft over a hardwired ethernet connection. This real-time data was completely separate from the Pixhawk Cube Orange, which operated independently. The SR-22 flight instrumentation included an Applanix Inertial Navigation System (INS) and a Garmin G600 Attitude and Heading Reference System (AHRS). On most flights, the air flow angle estimation algorithm was also run in real time on the laptop computer in the back of the aircraft, using only the real-time UDP data from the SR-22 flight instrumentation system. This was done to provide comparison data for the real-time results computed by the Pixhawk Cube Orange using its own sensor data.

The real-time calibration and air flow angle estimation algorithms were programmed, developed, and tested in Simulink, then auto coded onto the Pixhawk Cube Orange for flight testing using the MathWorks UAV Toolbox and support package for PX4 autopilots [24-26].

IV. Results

Air flow angle estimation results are described and shown using the F-16 nonlinear simulation and the instrumented Cirrus SR-22 aircraft in flight.

A. F-16 Nonlinear Simulation

The top two plots in Fig. 15 show flank angle and angle of attack estimates from the real-time air flow angle estimation algorithm, compared to simulated noisy measurements from the F-16 nonlinear simulation. White gaussian noise with RMS magnitude equal to 5 percent of the RMS value of each simulated output was used to simulate measurement noise.

The in-flight calibration was done when the learn flag was set to 1, as shown in the bottom plot of Fig. 15, during a pitch/yaw excitation maneuver. Then, the estimate flag was set to 1, which automatically set the learn flag to 0, marking the end of the in-flight calibration and the start of the real-time air flow angle estimation. The maneuvering in estimation mode was composed of random turns and pitch up/down maneuvers. The two plots at the top of Fig. 15 demonstrate the high accuracy of the real-time estimates of flank angle and angle of attack calculated by the real-time air flow angle estimation algorithm using noisy simulated flight data from the F-16 nonlinear simulation.

The third and fourth plots in Fig. 15 show that roll angle and dynamic pressure variations were significant during the time when the air flow angle estimation was active, demonstrating that changes in these flight variables did not adversely affect the accuracy of the real-time air flow angle estimation.

The RMS errors for the air flow angle estimates shown in Fig. 15 were 0.071 deg for flank angle and 0.074 deg for angle of attack. However, these values include the random measurement noise on the simulated F-16 flight data for the air flow angles plotted in Fig. 15. The RMS errors for the air flow angle estimates compared to noise-free data from the F-16 nonlinear simulation (not shown) were 0.053 deg for flank angle and 0.027 deg for angle of attack.

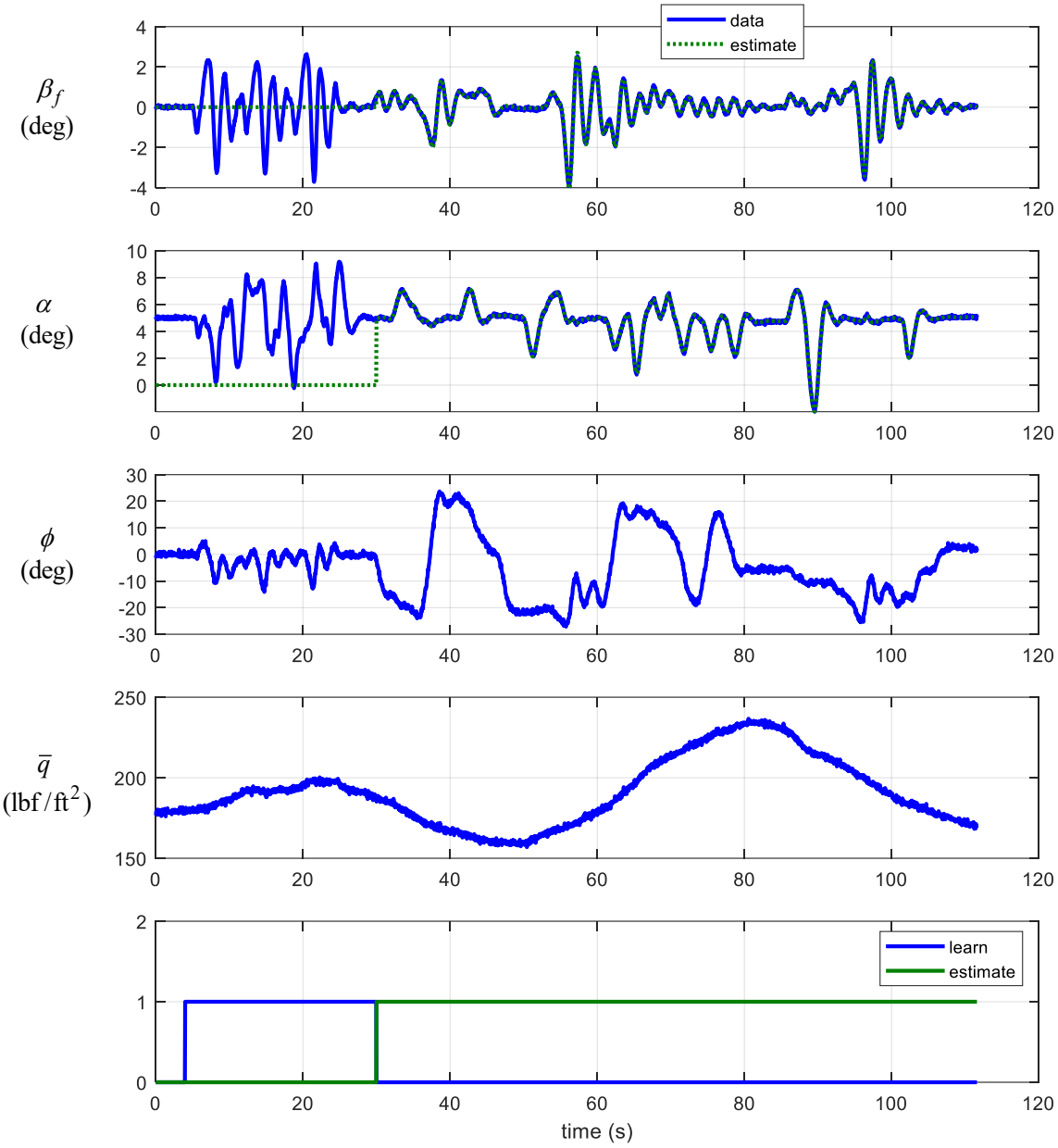


Figure 15. Data and air flow angle estimation results from F-16 nonlinear simulation

B. Cirrus SR-22 Flight Test

Figure 16 shows real-time air flow angle estimation results from the onboard Pixhawk Cube Orange running the algorithm developed in this work, compared to measured air flow angle data obtained from the vane sensors on the wing shown in Fig. 14. The results shown in Fig. 16 are in the same format and arrangement as in Fig. 15. The vane sensor data were time-synchronized with Pixhawk Cube Orange data during post-flight analysis to make the plots shown in Fig. 16.

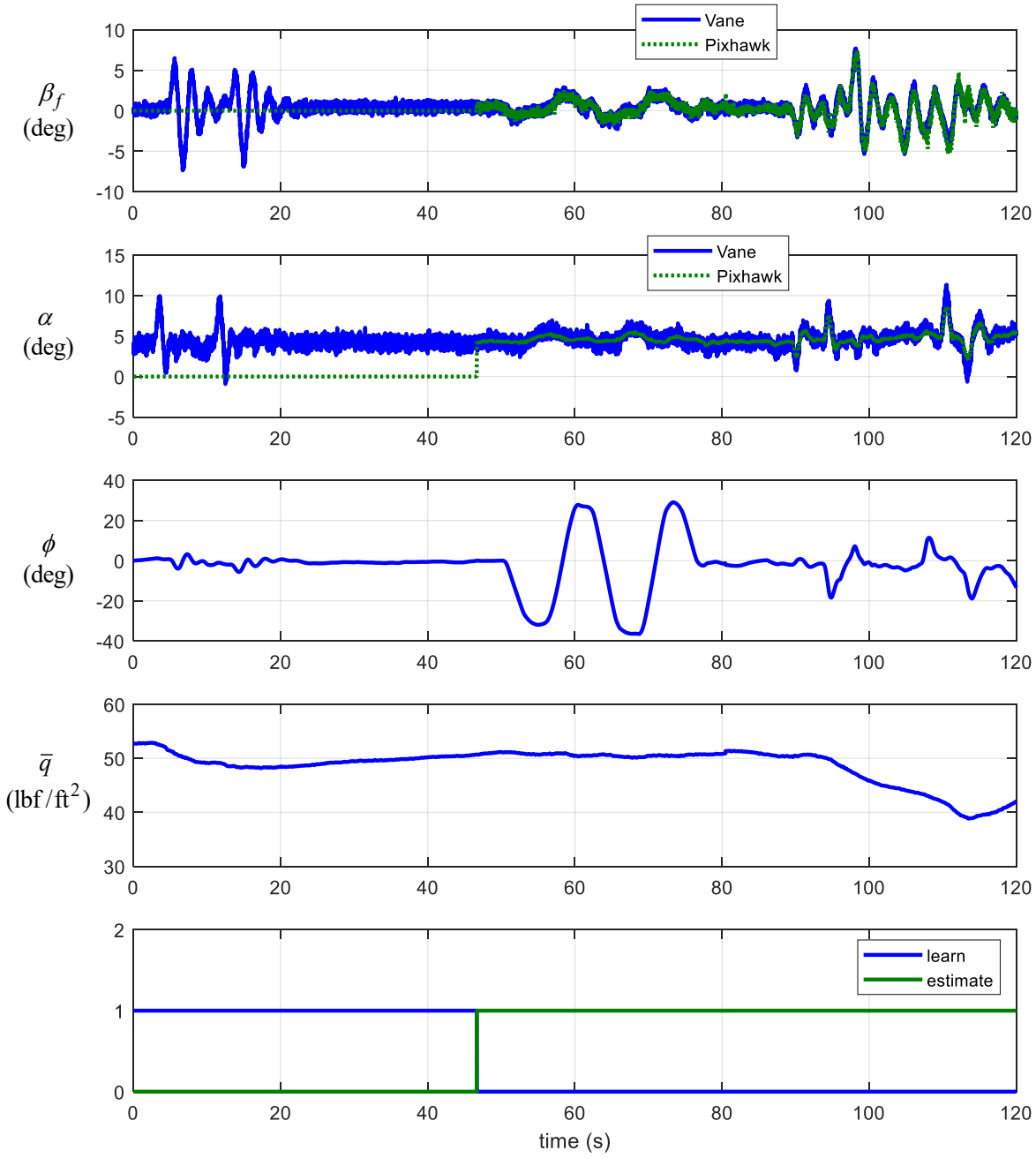


Figure 16. Data and air flow angle estimation results from SR-22 flight test

The Pixhawk Cube Orange was in calibration mode during the first part of the flight data record, with learn flag set to 1 and estimation flag set to 0. The pilot executed 2 pitch-yaw doublet sequences in calibration mode. Following that, the learn flag was turned off (set to 0), which automatically turned on the estimate flag (set to 1). This switched the Pixhawk Cube Orange into estimation mode and activated the real-time air flow angle estimation equations using model parameters determined in real time based on the flight data collected just previously in calibration mode, as indicated in Fig. 16. Note that the calibration maneuver was complete at approximately the 25 s mark, but the estimation mode was not activated until the 45 s mark, because the flight test engineer was completing other tasks. This delay did not affect the air flow model parameter estimates or the air flow angle estimates because the pilot was instructed to hold steady, so there was virtually no dynamic information in the flight data from 25 s until 45 s. Consequently, even though the real-time parameter estimation for air flow angle model calibration was running during this time period, the resulting parameter estimates were practically unchanged, as expected.

The noise on the measured air flow angle data from the vane sensors had contributions from engine/propeller vibrations acting on the composite monoplane construction of the aircraft, and also from the relatively close proximity of the vane sensors to the leading edge of the wing and the wingtip. This proximity probably caused local flow distortions and unsteady aerodynamics that affected the vane sensor measurements. Mismatches that could have been caused by such errors are most apparent near sudden large changes in angle of attack, such as during the time period from 110 s to 115 s.

The flank angle measurements from the vane sensor showed a bias error of -3.6 deg in steady, symmetric, wings-level flight at constant altitude. This bias in the flank angle vane measurement was from sidewash due to the proximity of the vane sensor to the right wing and fuselage. The flank angle measurements from the vane sensor shown in Fig. 16 have this bias removed. No such errors were present in the real-time air flow angle estimates from the Pixhawk Cube Orange.

The vane sensor measurements were corrected to the aircraft center of gravity using standard position correction equations [1,2]. Position corrections were not applied to the air flow angle estimates from the Pixhawk Cube Orange because of the proximity of the Pixhawk Cube Orange to the aircraft center of gravity. Note that if corrections were desired or required for a Pixhawk Cube Orange located significantly away from the aircraft center of gravity, the necessary angular rate and angular acceleration data were available inside the real-time algorithm to make such corrections using standard equations [1,2].

The noise on the air flow angle estimates came from the noise on the Pixhawk Cube Orange sensor data that were inputs to the estimation equations (36) and (38). Other filtering and smoothing techniques could be applied in real time to further reduce the noise on those signals, but generally at the cost of greater complexity and time delay in the resulting air flow angle estimates.

Although the Pixhawk Cube Orange had the analog-to-digital conversion capability necessary to use the dynamic pressure from onboard sensors, constraints on time and resources prevented this development. Consequently, the Pixhawk Cube Orange used an estimated dynamic pressure, computed as described earlier. The results shown in Fig. 16 are the result of using only the sensor data and computational capability available on the Pixhawk Cube Orange.

The plots in Fig. 16 demonstrate the accuracy of the real-time estimates of flank angle and angle of attack from the real-time air flow angle estimation algorithm, and also demonstrate that the results can be achieved onboard the aircraft in real time at 50 Hz using inexpensive Pixhawk Cube Orange hardware. Note that the calibration and operation of the real-time air flow angle estimation algorithm did not use the vane sensor measurements in any way. The vane sensor measurements were only used for comparison to the real-time air flow angle estimates from the Pixhawk Cube Orange.

The RMS difference between the air flow angle estimates and the vane measurements were 0.68 deg for the flank angle and 0.67 deg for the angle of attack. These errors included both the effects of noise in the sensor data from the Pixhawk Cube Orange and noise in the vane sensor measurements. In addition, the vane measurements showed evidence of wing and boom bending and unsteady aerodynamics, based on frequency-domain analysis. The real-time air flow angle estimates did not have these adverse effects, which also contributed to the RMS difference values.

The results shown in Fig. 16 are for the SR-22 in cruise configuration (flaps up, landing gear up). Similar air flow angle estimation results were obtained for the SR-22 in approach configuration (flaps half, landing gear up) and landing configuration (flaps full, landing gear down). However, the different aircraft configurations, along with changes in aircraft mass/inertia properties, resulted in different values for the air flow model parameters, as expected.

V. Discussion

The approach for obtaining real-time air flow angle data described and demonstrated in this work is very practical, because the air flow angle estimation algorithm is simple and robust, and it can be implemented using the sensor data and computational capability available on a small, lightweight, and inexpensive Pixhawk Cube Orange.

Novel aspects of the approach include the following:

1) Flank angle is used instead of the sideslip angle, which decouples the angle of attack model from the lateral air flow angle model.

2) Vertical body-axis aerodynamic force modeling is used instead of lift aerodynamic force modeling for angle of attack estimation, which avoids the need for a_x measurements and still achieves the goal of using a model with dominant angle of attack dependence. This is advantageous because a_x measurements generally have low signal-to-noise ratio and are affected by power level. Using vertical body-axis aerodynamic force modeling removes the effects of power level on the angle of attack estimation for aircraft with propulsive force directed along the *x* body axis, and reduces the effects of power level in other cases.

3) Angle of attack and flank angle are estimated with separate independent calculations running simultaneously in real time on a small, lightweight, and inexpensive Pixhawk Cube Orange at 50 Hz.

4) Angular acceleration terms are included in the vertical and lateral force modeling to avoid the need for control surface position measurements.

5) The formulation allows the use of nonlinear terms in the vertical and lateral force modeling, and includes estimates of bias and linear trend with time in the models.

6) Real-time modeling techniques are used for accurate in-flight air flow angle model calibration, which enables accurate real-time air flow angle estimation based on efficient in-flight model calibration that can be easily repeated to refine or update the models.

7) The real-time modeling includes a trend term to account for the drift in reconstructed air flow angle data used for the air flow angle model calibration. The model term associated with the drift is then discarded for air flow angle estimation, because the drift arises from bias errors in the accelerometer and rate gyro measurements used in the air flow angle data reconstruction.

8) Using perturbation values for the translational accelerations during the in-flight air flow angle model calibration and air flow angle estimation assigns the bias term in the model to the constant value of the air flow angle about which the calibration is valid. Accordingly, the calibration model is only accurate for a range of air flow angles where the calibration model is valid relative to the reference condition at the start of the calibration maneuver. However, this could be overcome by repeating the calibration at different reference conditions, for example, or by using more complex air flow angle models.

9) The algorithm includes efficient in-flight calibration, providing the capability for updates and expansion of the flight envelope for accurate air flow angle estimates. This can include aircraft configuration changes such as flap deflections and landing gear deployment, as well as loading changes, fuel burn, and manufacturing variations for individual airframes.

10) The real-time air flow angle estimation algorithm works in turbulence, wind gusts, and steady wind conditions, as well as in calm air, because the air flow angle models are calibrated using the dynamic response of the aircraft to changes in air flow angles.

11) In-flight calibration and onboard real-time operation were demonstrated using the Pixhawk Cube Orange hardware and flight data alone. No prior analysis, data, or models were required.

12) The algorithm can be applied using GPS data to estimate dynamic pressure, which avoids the need for dynamic pressure measurements. If a dynamic pressure sensor is available, then the algorithm can be applied without GPS data or in a GPS-denied environment.

13) Real-time data smoothing is used to generate low-noise data for the real-time modeling and air flow angle estimation.

14) The real-time air flow angle estimation algorithm uses simple calculations, and does not require complementary filtering or Kalman filtering to optimize the accuracy of the air flow angle estimator by blending results from more than one source. The algorithm does not require the selection or adjustment of any tuning parameters or noise levels by an analyst. The air flow angle calibration and estimation algorithms run in real time on a Pixhawk Cube Orange to provide real-time angle of attack and flank angle estimates at 50 Hz.

15) Flight test validation of the real-time air flow angle estimation algorithm was achieved on a piloted general aviation aircraft using Pixhawk Cube Orange hardware and independent measurements of angle of attack and flank angle from calibrated air flow angle vanes mounted on the wing.

Practical considerations for implementing and applying the air flow angle estimation algorithm using a Pixhawk Cube Orange mounted near the center of gravity of the aircraft are explained next.

1) More sophisticated air flow model structures and/or bookkeeping of the modeling results could be used to build an air flow angle estimation algorithm that produces accurate results over a wider range of aircraft configurations, flight conditions, and mass/inertia. Inverting the modeling equations to estimate air flow angles will be more complex if more complex air flow angle models are used for wider applicability.

2) The in-flight calibration strictly applies only to the particular aircraft used for the calibration maneuver. A more comprehensive approach would be to calibrate for different aircraft configurations and loadings, then select or interpolate the air flow angle model parameters according to aircraft configuration and the measured or estimated mass/inertia of the aircraft. The calibration data should be collected in relatively calm air, for accuracy of the air flow angle reconstructions. After the air flow angle models are calibrated, the air flow angle estimation can be executed in any wind conditions.

3) The angular acceleration data obtained by smooth differentiation of the angular rate data were by far the noisiest data used in the air flow angle estimation algorithm. However, the models in Eqs. (36) and (38) show that the angular acceleration data are divided by dynamic pressure, which mitigates the effects of the noisy angular acceleration data.

4) The air flow angle estimates from the real-time algorithm do not have the lag that typically is present when flight test instrumentation is based on pressure measurements and/or mounted on a boom ahead of the aircraft center of gravity. However, a lag of exactly 2 samples at 50 Hz was incurred from data smoothing implemented to reduce noise in the real-time data from the Pixhawk Cube Orange sensors.

5) The linear drift with time in the reconstructed air flow angle data is only involved in calibration mode, not in estimation mode, because the latter does not use time integration. There may be small errors in the estimated air flow angles when the angular rate or accelerometer measurements have small bias errors or when those biases drift with time, but this error occurs at each time instant where the biases occur, and there is no integration (or summing) of the small errors over time.

6) The linear model structures used in this development are an assumption for the air flow angle estimation technique. The limitations of this assumption can be overcome with repeated real-time modeling in various flight conditions, or by using more complex model structures with validity over a larger range of flight conditions. The basic concept remains the same, and the air flow angle model parameters still depend on aircraft configuration and mass/inertia properties. This is because the aircraft aerodynamics and dynamic motion are being calibrated in flight to be used for estimating air flow angle data.

7) Data compatibility analysis compares reconstructed air flow angle data to direct air flow angle measurements, such as angle of attack and flank angle measurements from vane sensors, to estimate instrumentation errors. Similarly, the in-flight calibration data, which is detrended reconstructed air flow angle data from a maneuver starting at steady level flight condition, is excellent for calibrating the air flow angle models. If an analogous data compatibility analysis were being done, the vane measurements would be corrected for bias errors (from mounting imperfections and static elastic deflections) and scale factor errors (from upwash and sidewash). Accelerometer and rate gyro measurements are typically corrected for bias errors only. In this work, the accelerometer biases are removed by starting the calibration maneuver at a precise steady level flight condition and estimating the biases accordingly. The rate gyro biases are removed by the PX4 state estimation algorithm onboard the Pixhawk Cube Orange. This allows simple real-time air flow angle reconstruction to provide the necessary data for air flow angle model calibration, assuming relatively calm winds. After the air flow angle models are calibrated, the wind and turbulence conditions can be arbitrary, because the aircraft responds dynamically to the associated changes in air flow angles.

8) Flight testing demonstrated that the Pixhawk Cube Orange sensors can operate in a flight test environment. The vibration level inside the fuselage of the SR-22 was relatively high, due to the composite construction of the airframe and the reciprocating engine powerplant.

9) The aerodynamic model is calibrated in the frequency band associated with dynamic motion of the aircraft. Consequently, the reconstructed air flow angle data will be accurate in that frequency range, and this is the desired behavior. Real-time data smoothing is used to remove wideband noise during both the calibration and estimation modes of the real-time algorithm operation.

10) The real-time air flow angle estimation approach described in this work can be very accurate and versatile particularly for fixed-wing aircraft with electric propulsion directed along the x body axis and equipped with a dynamic pressure sensor. This eliminates mass/inertia variations and also accurately accounts for dynamic pressure variations, which would make both the in-flight model calibration and the air flow angle estimation more accurate and general.

11) The real-time air flow angle estimates produced by the Pixhawk Cube Orange in flight were not visible to the pilot or flight test engineer during the flight tests, because those results were simply recorded in log files stored on the Pixhawk Cube Orange. However, Bluetooth, Robot Operating System (ROS), or other telemetry solutions could be applied to send the real-time air flow angle estimation results from the Pixhawk Cube Orange to a display in the cockpit or the back seats.

VI. Summary and Conclusions

An accurate and practical algorithm for estimating air flow angles in real time onboard a fixed-wing aircraft was developed and demonstrated using s small, lightweight, and inexpensive Pixhawk Cube Orange. The algorithm was first developed and demonstrated using an F-16 nonlinear simulation, then further developed and tested in flight using the subscale SEARCH-1 aircraft, and finally demonstrated in flight using a Cirrus SR-22 general aviation aircraft. Real-time air flow angle estimates were compared to air flow angle measurements obtained from vane sensors mounted on a wing boom. The novel algorithm combines kinematic reconstruction, GPS data, and real-time modeling for calibration of the aircraft dynamic response to air flow angles during dynamic flight tests in relatively calm air, then implements an inversion of the calibrated model to produce accurate estimates of air flow angles in real time.

Because of the small expense, size, and weight of the Pixhawk Cube Orange hardware, installation or retrofit on an aircraft is straightforward and practical. In addition, the real-time robust operation, accurate results, simple onboard calculations, in-flight calibration, and the fact that no sensors need to be mounted on the exterior of the aircraft make the approach useful and practical for inexpensive and accurate real-time air flow angle data in many important applications. Some examples are: flight control in arbitrary wind fields, efficient and effective stability and control flight testing without expensive and delicate air flow angle instrumentation, flight testing and flight control for hypersonic vehicles, low-cost onboard air flow angle sensing in GPS-denied environments, and flight safety for commercial, military, and general aviation aircraft.

Acknowledgments

The efforts of the flight test team at NASA Langley Research Center in preparing the SR-22 aircraft and associated systems, carefully calibrating the instrumentation, and carrying out the flight operations to collect the high-quality flight data used in this study, are gratefully acknowledged. The team was composed of pilots Taylor Thorson and Pat Bookey, systems engineer Rick Yasky, flight instrumentation engineer Charles Howell, flight instrumentation software engineer Brent Pickering, flight test engineer Gene Morelli, and crew chief Mike Barnes.

Developmental flight testing was also done at NASA Langley Research Center using the SEARCH-1 subscale aircraft. The flight test team for that work included Mark Motter, Gene Morelli, Jody Miller, Greg Howland, Ben Simmons, Mario Smith, Garrett Asper, Jake Revesz, Matt Coldsnow, Dustin Schmitt, Jake Schaefer, Skyler Hudson, Braydon Chamberlain, Jen Fowler, Patrick Hill, and Ron Busan.

This research was funded by the NASA Langley Center Innovation Fund (CIF) / Internal Research and Development (IRAD) initiative, and the NASA Flight Demonstration and Concepts (FDC) project. Special thanks to Dan Williams, Deputy Director of the NASA FDC project, for his strong support and advocacy of the project and the associated flight testing on both the SEARCH-1 and SR-22 aircraft.

References

1. Morelli, E.A. and Klein, V. *Aircraft System Identification - Theory and Practice*, 2nd Edition, Sunflyte Enterprises, Williamsburg, VA, December 2016.
2. Grauer, J.A. and Morelli, E.A. "Some Common Discrepancies, Misnomers, and Misunderstandings in Aircraft Stability and Control," AIAA-2026-1882, *2026 AIAA SciTech Forum*, Orlando, FL, January 2026.
3. Hearing, E.A., Jr. "Airdata Measurement and Calibration," NASA TM 104316, December 1995.
4. Colgren, R.D., Frye, M.T., and Olson, W.M. "A Proposed System Architecture for Estimation of Angle of Attack and Sideslip Angle," AIAA 1999-4078, *AIAA Guidance, Navigation, and Control Conference and Exhibit*, Portland, OR, August 1999.
5. Colgren, R.D. and Martin, K.E. "Flight Test Validation of Sideslip Estimation Using Inertial Accelerations," AIAA 2000-4448, *AIAA Guidance, Navigation, and Control Conference and Exhibit*, Denver, CO, August 2000.
6. Lerro, A., Brandl, A., and Gili, P. "Model-Free Scheme for Angle-of-Attack and Angle-of-Sideslip Estimation, *Journal of Guidance, Control, and Dynamics*, Vol. 44, No. 3, March 2021, pp. 595-600.
7. Sarmento, A.G.P., de Souza, A.G., Góes, L.C.S., and da Silva, R.G.A. "Synthetic Estimation of Angle of Attack and Sideslip Using a Maneuver Reconstruction Method for Flight Testing of an UAV," *26th International Congress of Mechanical Engineering*, Virtual Congress, November 2021.
8. Zeis, J.E., Lambert, H.H., Calico, R.A., and Gleason, D. "Angle of Attack Estimation Using an Inertial Reference Platform," AIAA 88-4351, *AIAA 15th Atmospheric Flight Mechanics Conference*, Minneapolis, MN, August 1988.
9. Zeis, J.E. "Angle of Attack and Sideslip Estimation Using an Inertial Reference Platform," MS Thesis, AFIT/CAE/AA/88J-2, Air Force Institute of Technology, Wright-Patterson AFB, OH, 1988.
10. Wise, K.A. "Flight Testing of the X-45A J-UCAS Computational Alpha-Beta System," AIAA 2000-6215, *AIAA Guidance, Navigation, and Control Conference and Exhibit*, Keystone, CO, August 2006.
11. Lie, F.A.P. and Gebre-Egziabher, D. "Synthetic Air Data System," *Journal of Aircraft*, Vol. 50, No. 4, July-August 2013, pp. 1234-1249.
12. Valasek, J., Harris, J., Pruchnicki, S., McCrink, M., Gregory, J., and Sizoo, D.G. "Derived Angle of Attack and Sideslip Angle Characterization for General Aviation," *Journal of Guidance, Control, and Dynamics*, Vol. 43, No. 6, June 2020, pp. 1039-1055.
13. Heller, M., Myschik, S., Holzapfel, F., and Sachs, G. "Low-Cost Approach Based on Navigation Data for Determining Angles of Attack and Sideslip for Small Aircraft," AIAA 2003-5777, *AIAA Guidance, Navigation, and Control Conference and Exhibit*, Austin, TX, August 2003.
14. Cervia, F., Denti, E., Galatolo, R., and Schettini, F. "Air Data Computation in Fly-by-Wire Flight Control Systems," *Journal of Aircraft*, Vol. 43, No. 2, Mar.–Apr. 2006, pp. 450–455. doi:10.2514/1.16270
15. Martos, B. and Rogers, D.F. "Low-Cost Accurate Angle-of-Attack System," *Journal of Aircraft*, Vol. 55, No. 2, March-April 2018.

16. Lerro, A., Battipede, M., Gili, P., and Brandl, A. "Survey on a Neural Network for Non Linear Estimation of Aerodynamic Angles," *IEEE Intelligent Systems Conference*, London, UK, September 2017, pp. 929-935.

17. Mohamed, M. and Joy, N. "Nonlinear Filter and Neural Modeling for Calibration of Aircraft Airdata System," *Journal of Aerospace Information Systems*, Vol. 18, No. 12, December 2021.

18. Oosterom, M. and Babuška, R. "Virtual Sensor for the Angle-of-Attack Signal in Small Commercial Aircraft," *IEEE International Conference on Fuzzy Systems*, Vancouver, BC, Canada, July 2006, pp. 1396-1403.

19. NASA Software Catalog, https://software.nasa.gov/software/LAR-16100-1, accessed 10 July 2025.

20. Morelli, E.A. and Klein, V. "Application of System Identification to Aircraft at NASA Langley Research Center," *Journal of Aircraft*, Vol. 42, No. 1, January-February 2005, pp. 12-25.

21. Morelli, E.A. and Grauer, J.A. "Practical Aspects of Frequency-Domain Approaches for Aircraft System Identification," *Journal of Aircraft*, Vol. 57, No. 2, March 2020, pp. 268-291.

22. Morelli, E.A. and Grauer, J.A. "Advances in Aircraft System Identification at NASA Langley Research Center," *Journal of Aircraft*, Vol. 60, No. 5, September-October 2023, pp. 1354-1370.

23. Morelli, E.A. "Real-Time Aerodynamic Parameter Estimation without Air Flow Angle Measurements," *Journal of Aircraft*, Vol. 49, No. 4, July-August 2012, pp. 1064-1074.

24. UAV Toolbox, https://www.mathworks.com/help/uav/, accessed 24 April 2024.

25. Asper, G.D. and Simmons, B.M. "Rapid Flight Control Law Deployment and Testing Framework for Subscale VTOL Aircraft," NASA/TM-20220011570, September 2022.

26. Simmons, B. M., Ackerman, K. A., Asper, G. D., Gray, M. N., Snyder, S. M., Axten, R. M., Geuther, S. C., and Chan, R., "Subscale Tiltrotor eVTOL Aircraft Dynamic Modeling and Flight Control Software Development," *Vertical Flight Society, 81st Annual Forum & Technology Display*, Virginia Beach, VA, May 2025.